Rapid Li^+ transport within the MOF-based composite solid electrolyte enables High-Performance FeS_2-Based Quasi-Solid-State Batteries

Yaxin Wang,[a] Yanhui Zhang,[a] Ting Ma,[a] Yanjun Cai,*[a] Hualing Tian,[a] Xiang Yao,[a] Yingbo Wang,[a] Zhi Su*[a, b]

[a] College of Chemistry and Chemical Engineering, Xinjiang Key Laboratory of Energy Storage and Photoelectroctalytic Materials, Xinjiang Normal University, Urumqi, 830054, Xinjiang, P. R. China. E-mail: cyjxjsf@yeah.net, suzhi@xju.edu.cn

[b] College of Chemical Engineering, Xinjiang Industry Technical College, Urumqi, 830021, Xinjiang, P.R. China

Preparation of CPE with different ratios

The solution was prepared by first dissolving 0.85 g and 0.95 g of PAN, respectively, in 10 mL of anhydrous DMF, followed by the successive addition of 0.15 g and 0.05 g of La-MOF, 0.015 g of TiO_2, and 0.2 g of LiTFSI, with intermittent stirring after each addition. All procedures were carried out in an argon-atmosphere glove box (H_2O/O_2 < 1 ppm). Electrospinning was performed under the following conditions: a voltage of 18 kV, a feed rate of 0.15 $mm \cdot min^{-1}$, a collection distance of 20 cm, and a controlled relative humidity of 55-60%. The collected membrane was finally vacuum-dried at 60 ℃ for 6 h.

Synthesis of FeS_2 materials

All chemicals were used as received without further purification. The FeS_2

cathode material employed in this experiment was synthesised via the hydrothermal method. Dissolve 2.40 g of $Na_2S•9H_2O$ in 40 mL of deionised water, then add 0.32 g of ground sublimed sulphur. Place the solution on a magnetic stirrer and maintain stirring at 80 °C for 6 h. Once the solution turned clear yellow, the precursor solution was prepared. Subsequently, 2.78 g of $FeSO_4•7H_2O$ was dissolved in 20 mL of deionised water. Under magnetic stirring at room temperature, the precursor solution from the first step was added dropwise using a pipette, with continuous stirring throughout. Once the precursor solution was fully incorporated, the mixture was transferred to a PTFE-lined vessel. The PTFE-lined vessel was placed on a magnetic stirrer and stirred at 60 °C for 30 minutes. Subsequently, the mixture was placed in a 100 mL stainless steel autoclave and maintained at 200 °C for 12 h. Allow the mixture to cool naturally to room temperature. Thoroughly wash the samples with deionised water and ethanol respectively, then dry in an oven at 60 °C for 24 h. The final product, FeS_2, is obtained in powder form.

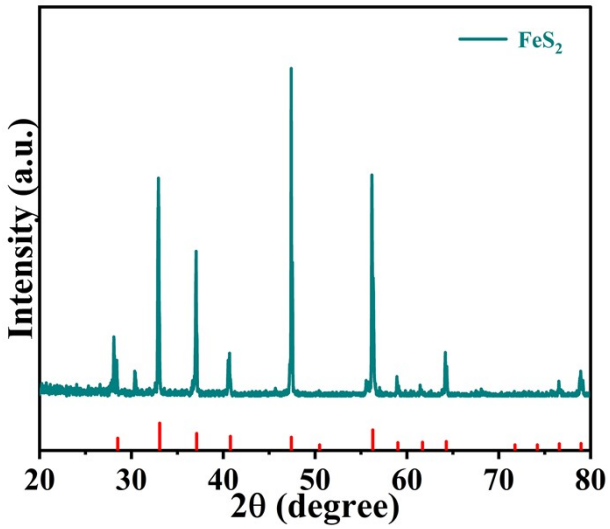

Fig. S1 XRD spectrum of FeS_2

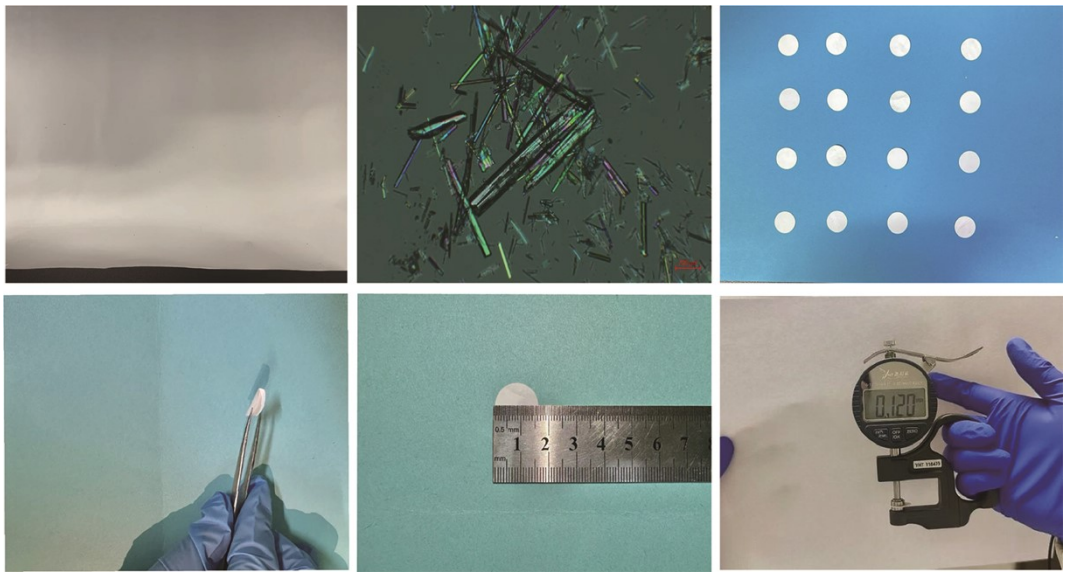

Fig. S2 The optical image of La-MOF-PAN composite solid-state electrolyte

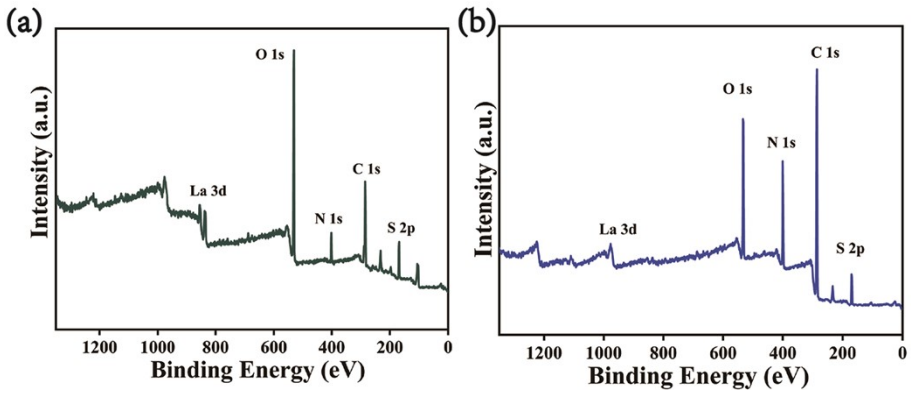

Fig. S3 XPS spectra of La-MOF and La-MOF-PAN

Single crystal X-ray diffraction

The diffraction data were collected at room temperature on a Bruker SMART APEX III 4K CCD diffractometer and Mo Kα radiation (λ=0.71073 Å). The data was integrated by APEX III, and the multi-scan method was used for the absorption corrections. The crystal structures of the four compounds were determined by the direct methods and refined by full-matrix least-squares fitting on F^2 using the

SHELXS crystallographic software package on the Olex2 program.[1, 2] All atoms except H were refined with anisotropic displacement parameters. The structure was checked by PLATON, and no higher symmetry was found.[3] The crystallographic data and structure refinement are tabulated in Table S1.

Table S1 Crystal data and structure refinement for $La(COOH)_3$

Empirical formula	$La(COOH)_3$
Formula weight	273.96
Temperature	298 K
Wavelength	0.71073 Å
Crystal system, space group	Trigonal, *R*3
Unit cell dimensions	a = 10.7286(6) Å α = 90 ° b = 10.7286(6) Å β = 90 ° c = 4.1382(4) Å γ = 120 °
Volume	412.50(6) $Å^3$
Z	3
Calculated density	3.309 $Mg·m^{-3}$
Absorption coefficient	7.732 mm^{-1}
F (000)	378
Crystal size	0.1 × 0.09 × 0.03 mm^3
Theta range for data collection	3.80 to 30.60 °
Limiting indices	$-15 \le h \le 15, -15 \le k \le 15, -5 \le l \le 5$
Reflections collected / unique	10574 / 564 [R_{int} = 0.0439]
Data / restraints / parameters	564 / 1 / 31
Goodness–of–fit on F^2	1.164
Final *R* indices [$I > 2\sigma(I)$] [a]	R_1 = 0.0079, wR_2 = 0.0191
R indices (all data) [a]	R_1 = 0.0079, wR_2 = 0.0191
Largest diff. peak and hole	0.2 and -0.56 $Å^{-3}$
Flack parameter	0.013(12)

[a] $R_1 = \Sigma||F_o| - |F_c||/\Sigma|F_o|$ and $wR_2 = [\Sigma w(F_o^2 - F_c^2)^2 / \Sigma w F_o^4]^{1/2}$ for $F_o^2 > 2\sigma(F_o^2)$

Table S2 Analysis Table of Specific Surface Area and Pore Structure Parameters for La-MOF Materials

Sample	S_{BET} (m^2g^{-1})	S_{mic} (m^2g^{-1})	S_{mes} (m^2g^{-1})	S_{mes}/S_{BET} (%)	V_{total} (cm^3g^{-1})	V_{mic} (cm^3g^{-1})	V_{mes} (cm^3g^{-1})
La-MOF	2.418	0.127	2.291	0.948	0.01	5.9×10^{-5}	0.01

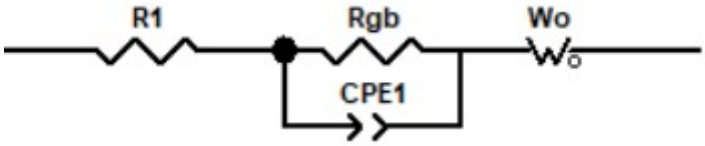

Fig. S4 Equivalent circuit diagram of La-MOF-PAN composite solid-state.

Table S3 Ion conductivity of La-MOF-PAN at 25–80 °C

T(°C)	d(cm)	R_g	R_{gb}	R	σ (Rg)(S cm^{-1})	σ (R_{gb})(S cm^{-1})	σ (R)(S cm^{-1})
25	0.012	58.3	105.8	164.1	1.02×10^{-4}	5.64×10^{-5}	3.63×10^{-5}
30	0.012	43.5	95.5	139.0	1.37×10^{-4}	6.25×10^{-5}	4.29×10^{-5}
40	0.012	34.5	88.4	122.9	1.73×10^{-4}	6.75×10^{-5}	4.85×10^{-5}
50	0.012	27.6	43.6	71.2	2.16×10^{-4}	1.36×10^{-4}	8.38×10^{-5}
60	0.012	11.8	9.9	21.7	5.06×10^{-4}	6.03×10^{-4}	2.75×10^{-4}
70	0.012	8.7	8.2	16.9	6.86×10^{-4}	7.28×10^{-4}	3.53×10^{-4}
80	0.012	5.4	6.3	11.7	1.10×10^{-3}	9.48×10^{-4}	5.10×10^{-4}

$R= R_g+R_{gb}$, R_g is intra-grain and R_{gb} inter-grain.

we add the ionic conductivity data for the pure PAN electrolyte. The test data, as shown in the Fig. S4 and Table S4, reveal that at 60 °C, the conductivity of La-MOF-PAN (2.75×10^{-4} S cm^{-1}) is an order of magnitude higher than that of pure PAN

(~5.12×10^{-5} S cm^{-1}). This addition will provide direct evidence supporting the conclusion that La-MOF significantly enhances ionic conductivity. The introduction of La-MOF substantially improves the intrinsic ionic conductivity of the electrolyte, and the system maintains good thermal stability.

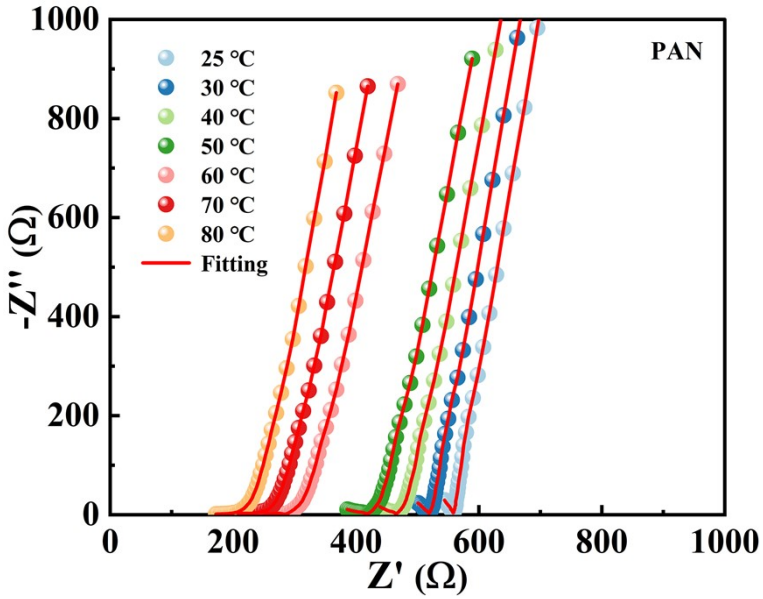

Fig. S5 AC impedance plots of PAN solid electrolyte at 30-80 °C.

Table S4 Ionic conductivity of PAN at 25-80 °C

T(°C)	d(cm)	R_g	R_{gb}	R	σ (Rg)(S cm^{-1})	σ (R_{gb})(S cm^{-1})	σ (R)(S cm^{-1})
25	0.039	362	198	560	5.36×10^{-5}	9.80×10^{-5}	3.46×10^{-5}
30	0.039	327	193	520	5.93×10^{-5}	1.01×10^{-4}	3.73×10^{-5}
40	0.039	300	165	467	6.47×10^{-5}	1.18×10^{-4}	4.15×10^{-5}
50	0.039	276	148	424	7.03×10^{-4}	1.31×10^{-4}	4.58×10^{-5}
60	0.039	182	115	297	1.07×10^{-4}	1.69×10^{-4}	6.53×10^{-5}
70	0.039	165	87	252	1.18×10^{-4}	2.23×10^{-4}	7.69×10^{-5}
80	0.039	147	72	219	1.32×10^{-4}	2.69×10^{-4}	8.86×10^{-5}

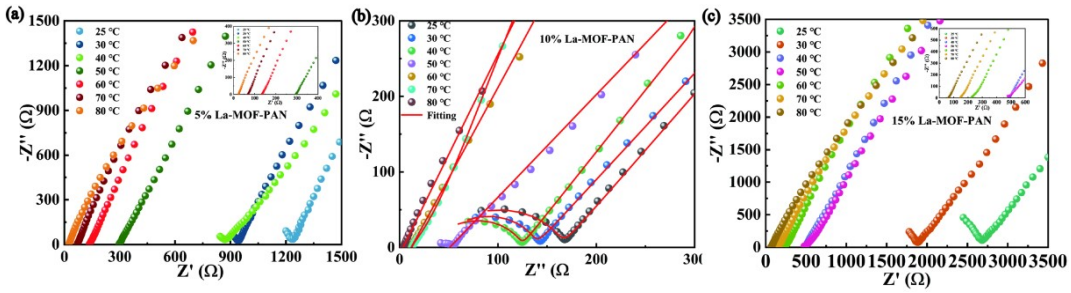

Fig. S6 Ionic conductivity of La-MOF-PAN composite solid-state electrolyte(a) 5 wt%, (b) 10 wt%, (c) 15 wt%.

Ionic conductivity is a critical parameter for evaluating solid-state electrolytes. The ionic conductivity of the composites with varying La-MOF content was investigated from 25 °C to 80 °C using electrochemical impedance spectroscopy (EIS), as shown in Fig. 2(a-c). The ionic conductivity was calculated using the formula $\sigma = d/(R_b \times S)$. At 25 °C, the ionic conductivities for 5 wt%, 10 wt%, and 15 wt% La-MOF-PAN composites are 7.22×10^{-6}, 3.63×10^{-5}, and 2.97×10^{-6} S cm^{-1}, respectively. When the temperature increases to 60 °C, the corresponding values become 6.35×10^{-5}, 2.75×10^{-4}, and 3.06×10^{-5} S cm^{-1}.

The results indicate that when the La-MOF content increases from 5 wt% to 10 wt%, the ionic conductivity improves significantly. In contrast, a further increase to 15 wt% leads to a notable decrease in conductivity. This trend suggests that an insufficient amount of La-MOF (5 wt%) fails to establish a continuous and efficient network for ions transport within the PAN matrix, resulting in high bulk and grain boundary resistance. At the optimal content of 10 wt%, the dispersion of La-MOF and the formation of interconnected ion-conducting pathways reach the best balance. This facilitates smoother ion migration through the bulk material, leading to the highest overall ionic conductivity. However, an excessive amount of La-MOF (15 wt%) may cause particle agglomeration, which disrupts the homogeneous microstructure, hinders polymer chain segmental motion, and reduces ion mobility. These factors collectively increase the total resistance, thereby lowering the ionic conductivity.

5 wt% La-MOF:

Table S5 Ion conductivity of 5% La-MOF-PAN at 25-80 °C

T(°C)	25	30	40	50	60	70	80
d (cm)	0.018	0.018	0.018	0.018	0.018	0.018	0.018
R	1240	947	874	303	141	75	28
σ (S cm^{-1})	7.22×10^{-6}	9.46×10^{-6}	1.02×10^{-5}	2.96×10^{-5}	6.35×10^{-5}	1.19×10^{-4}	3.20×10^{-4}

δ=d/RS, S=2.01 cm^2

10 wt% La-MOF:

Table S6 Ion conductivity of 10% La-MOF-PAN at 25-80 °C

T (°C)	25	30	40	50	60	70	80
d (cm)	0.014	0.014	0.014	0.014	0.014	0.014	0.014
R	164	139	123	71	22	17	12
σ (S cm^{-1})	4.25×10^{-5}	5.01×10^{-5}	5.66×10^{-5}	9.81×10^{-5}	3.17×10^{-4}	4.09×10^{-4}	5.80×10^{-4}

δ=d/RS, S=2.01 cm^2

15 wt% La-MOF:

Table S7 Ion conductivity of 15% La-MOF-PAN at 25-80 °C

T (°C)	25	30	40	50	60	70	80
d (cm)	0.012	0.012	0.012	0.012	0.012	0.012	0.012
R	2680	1890	494	482	229	147	64
σ (S cm^{-1})	2.23×10^{-6}	3.16×10^{-6}	1.21×10^{-5}	1.24×10^{-5}	2.61×10^{-5}	4.06×10^{-5}	9.33×10^{-5}

δ=d/RS, S=2.01 cm^2

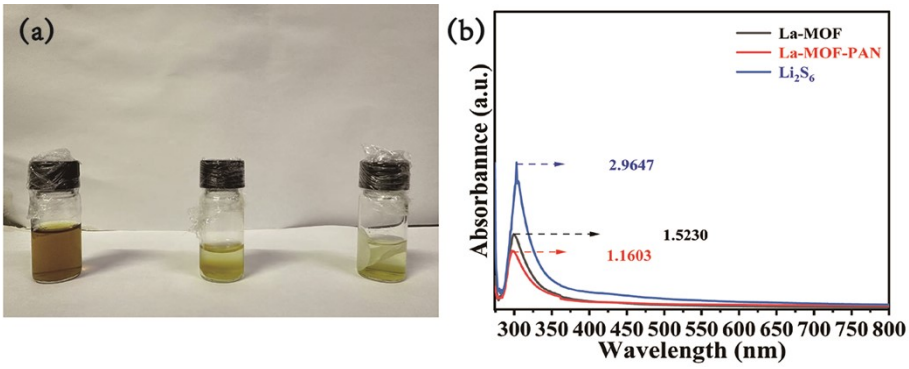

Fig.S7 Optical photographs and UV-vis absorption spectra of polysulfide adsorption

experiments for pristine Li_2S_6 solution, La-MOF material, and La-MOF-PAN

To investigate the adsorption capacity of La-MOF toward Li_2S_6, polysulfide adsorption experiments were designed (Figure S8). In an Ar-filled glove box, 20 mg of La-MOF and La-MOF-PAN were separately added to sealed vials containing 5 mmol of Li_2S_6 solution and left to stand for 12 hours. The figure clearly shows that compared to the Li_2S_6 solution without any adsorbent, the supernatant with C/S/HES^{-1} turned from yellow to nearly clear and transparent. The supernatants with La-MOF and La-MOF-PAN exhibited significant decoloration, attributed to the strong adsorption capacity of La-MOF toward polysulfides. Similarly, UV spectroscopy analysis of the supernatants revealed absorption peak intensities at 312 nm of 2.9647 for Li_2S_6, 1.5230 for La-MOF, and 1.1603 for La-MOF-PAN. The absorption peak intensity at 312 nm was significantly reduced in Li_2S_6 with La-MOF-PAN added, followed by La-MOF. These results indicate that the La-MOF-PAN composite solid electrolyte exhibits strong adsorption capacity for polysulfides.

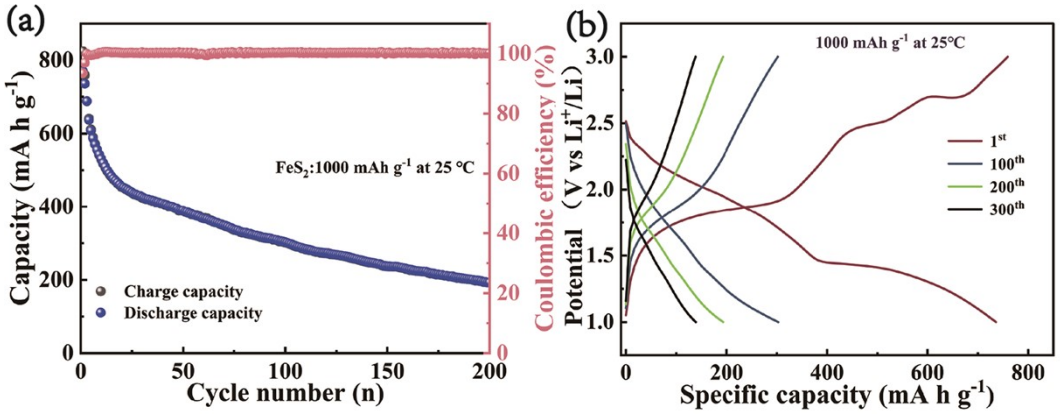

Fig. S8 Electrochemical performance of Li|La-MOF-PAN|FeS_2 and Li| PAN|FeS_2 in LIBs cycling at 1000 mA g^{-1}.

Table S8 Literature review of CPEs and the corresponding electrochemical performance in batteries.

Electrolyte	Composites cathode	Ionic conductivity(S cm^{-1})	Electrochemical performance of the battery	Refs.
$Li_7P_3S_{11}$	FeS_2@C/rGO@10%$Li_7P_3S_{11}$ and SuperP	/	350.3mAhg^{-1} at 0.5C	[5]
Li_6PS_5Cl	Integrated 3D FeS_2	2.6×10^{-3}S cm^{-1} at RT	667 mAh g^{-1} at 1C	[6]
$Li_7P_3S_{11}$	FeS_2@$Li_7P_3S_{11}$ @CNT	1.27×10^{-3} S cm^{-1} at RT	capacity of 284.8 mAh g^{-1} at 0.1C with	[7]

				52.4% capacity retention after 80 cycles	
Li_6PS_5Cl	FeS_2,Li_6PS_5Cl,carbonblack	2.7×10^{-3} cm^{-1}	S	The initial discharge capacity of 760 mAh g^{-1}	[8]
$Li_{5.5}PS_{4.5}Cl_{1.5}$	FeS_2@MWCNT, SuperP	5.38×10^{-3} cm^{-1}	S	Capacity of 418.9 mAh g^{-1} at 50 mA g^{-1} after 200 cycles	[9]
$Li_{6.8}Si_{0.8}As_{0.2}S_5$ I	FeS_2, $Li_{6.8}Si_{0.8}As_{0.2}S_5I$	1.04×10^{-2} cm^{-1} at 30°C	S	The initial capacity of 835.2 mAh g^{-1} at 0.1C	[10]
Li_6PS_5Cl-wt% PTFE	FeS_2@C/rGO,Li_6PS_5Cl	2.2×10^{-3} cm^{-1}	S	Capacity of 370.7 mAh g^{-1}	[11]

			at 0.3C after 200 cycles	
La-MOF-PAN	FeS_2	2.75×10^{-4} S cm^{-1} at 60 °C	The initial discharge specific capacity of the cell was 828 mAh g^{-1} at 500 mAh g^{-1} and 686 mAh g^{-1} after 400 cycles	This work

we assembled quasi-solid-state Li|La-MOF-PAN|FeS_2 coin cells with active material loadings of 0.98, 1.52, and 1.98 mg cm^{-2}, respectively. Their cycling performance was evaluated at the same current density of 500 mA g^{-1}, and the results are presented in the Fig. S9.

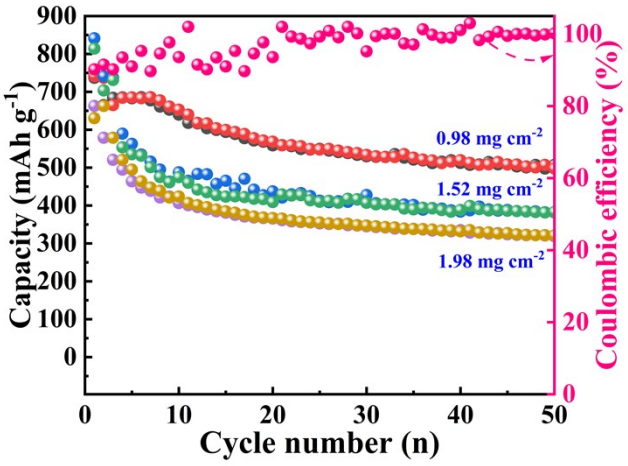

Fig. S9 Quasi-solid-state Li|La-MOF-PAN|FeS_2 batteries with varied active material loadings

As the FeS_2 loading increased from 0.98 mg cm^{-2} to 1.98 mg cm^{-2}, the initial discharge capacity showed a decreasing trend (~748 mAh g^{-1} at 0.98 mg cm^{-2} vs. ~661 mAh g^{-1} at 1.98 mg cm^{-2}). This is primarily attributed to the increased electrode thickness at higher loadings, which elongates the ion/electron transport pathways and enhances polarization, thereby reducing the utilization of the active material. Despite this, all high-loading cells demonstrated good cycling stability with slow capacity fading over 50 cycles. Even at the highest loading of 1.98 mg cm^{-2}, the cell maintained stable cycling performance with a high capacity retention rate after 50 cycles. This indicates that the quasi-solid-state electrolyte system effectively suppresses side reactions and the shuttle effect. The advantage stems from the La-MOF-PAN quasi-solid composite electrolyte: its three-dimensional structure facilitates uniform lithium-ion transport while mitigating the volume change of the high-loading electrode and interfacial side reactions.

Although the theoretical capacity of FeS_2 is 894 mAh g^{-1}, the lower practical

capacities observed in high-loading coin cells are common in such systems, mainly due to the limited ion diffusion kinetics in thick electrodes, which prevents part of the active material from being fully utilized.

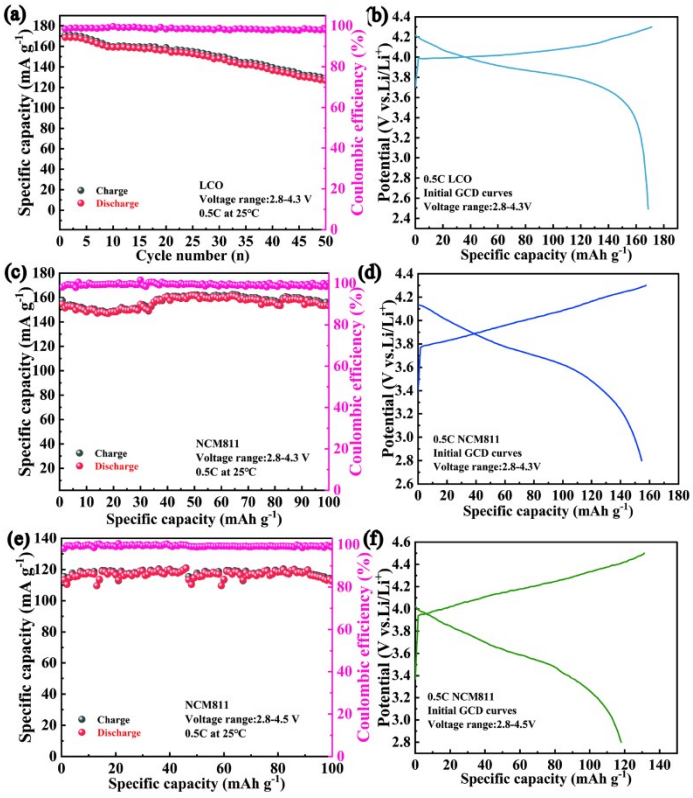

Fig. S10 (a) Li|La-MOF-PAN|LCO cyclic performance at a voltage window of 2.8-4.3 V and a rate of 0.5 C,(b) initial charge-discharge curve, (c) Li|La-MOF-PAN |NCM811 cycling performance at conventional voltages of 2.8-4.3 V and a 0.5 C charge rate, (d) initial charge-discharge curve, (e) Li|La-MOF-PAN|NCM811 cycling performance at high voltage (2.8-4.5 V) and 0.5 C rate, (f) initial charge-discharge curve.

The linear sweep voltammetry (LSV) result confirms the stability of the material within a voltage window of 5.06 V, indicating that the synthesized composite electrolyte is potentially suitable for high-voltage cathode materials. Accordingly, we

assembled half-cells with commercial high-voltage cathodes (LCO and NCM811).

Fig. S10 (a) presents the cycling performance of the Li|La-MOF-PAN|LCO cell within a voltage window of 2.8-4.3 V at a rate of 0.5 C. The LCO cathode delivered an initial discharge specific capacity of approximately 170 mA h g^{-1}. A high capacity retention was maintained after 100 cycles, demonstrating stable cycling characteristics. The coulombic efficiency consistently remained close to 100%, indicating high reversibility and minimal side reactions during the charge/discharge processes. Fig. S10 (b) displays the first-cycle charge/discharge profiles of Li|La-MOF-PAN|LCO (2.8-4.3 V, 0.5 C). The smooth curves exhibit the typical LCO plateau features. Following charging to 4.3 V, a stable discharge plateau is observed, accompanied by a high initial coulombic efficiency, further evidencing stable electrolyte|LCO interfaces at moderately high voltages.

Fig. S10 (c) shows the cycling performance of Li|La-MOF-PAN|NCM811 in a conventional voltage range (2.8-4.3 V) at 0.5 C. The NCM811 cathode achieved an initial discharge capacity near 190 mAh g^{-1}, which is higher than that of LCO under identical conditions, reflecting its intrinsic advantage of high specific capacity. Excellent capacity retention was observed after 100 cycles. Fig. S10 (d) depicts the corresponding first-cycle charge/discharge profiles for NCM811 (2.8-4.3 V, 0.5 C), showing the distinct high and low voltage plateaus characteristic of NCM811 with normal shape and no abnormal polarization.

Fig. S10 (e) presents the cycling performance of Li|La-MOF-PAN|NCM811 at a high cut-off voltage (2.8-4.5 V, 0.5 C). The initial discharge capacity of NCM811

significantly increased to approximately 212 mA h g^{-1}. Although capacity fade occurred over 200 cycles, the capacity was maintained at a relatively high level. Fig. S10 (f) shows the corresponding first-cycle charge/discharge profiles at 2.8-4.5 V and 0.5 C. Even within the high-voltage region up to 4.5 V, the charge/discharge profiles remained well-formed.

In all tests, the coulombic efficiency rapidly reached and remained at nearly 100%. This suggests that the composite solid electrolyte forms relatively stable, low-impedance solid-solid interfaces with both cathode materials, enabling efficient Li^+ transport and effectively suppressing persistent interfacial side reactions.

In summary, this set of figures provides strong evidence that: 1) The La-MOF-PAN composite solid electrolyte possesses the key characteristics required for application with high-voltage cathode materials (wide electrochemical window, good interfacial stability). 2) This electrolyte exhibits good compatibility with commercial high-voltage cathodes (LCO and NCM811), supporting the realization of their high specific capacities and stable cycling performance.

We assembled a quasi-solid-state Li|La-MOF-PAN|FeS_2 cell, which was left to stand for 12 h before conducting charge-discharge tests within a voltage range of 1-3 V at a current density of 200 mAh g^{-1}. The XPS measurements were performed on the cell at the OCV state, after discharging to 1 V, and after charging to 3 V. The following analysis based on these data will provide an in-depth examination to demonstrate that the interfacial side products have been adequately characterized and

the stability of the FeS_2 cathode has been verified.

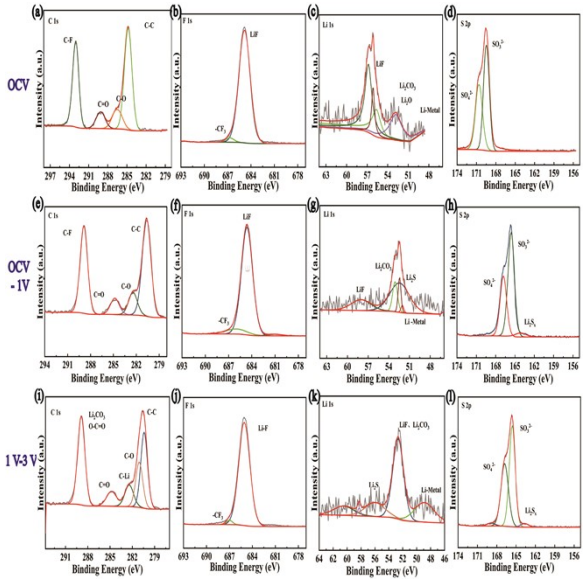

Fig. S11 XPS data of the lithium metal anode (a) C 1s, (b) F 1s, (c) Li 1s, (d) S 2p at OCV; (e) C 1s, (f) F 1s, (g) Li 1s, (h) S 2p upon discharging from OCV to 1 V; (i) C 1s, (j) F 1s, (k) Li 1s, (l) S 2p upon charging from 1 V to 3 V.

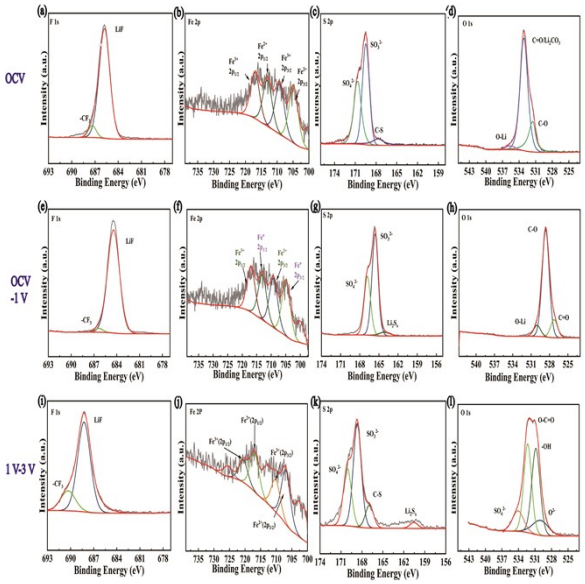

Fig. S12 XPS data of the FeS_2 cathode (a) F 1s, (b) Fe 2p, (c) S 2p, (d) O 1s at OCV; (e) F 1s, (f) Fe 2p, (g) S 2p, (h) O 1s upon discharging from OCV to 1 V; (i) F 1s, (j) Fe 2p, (k) S 2p, (l) O 1s upon charging from 1 V to 3 V.

The XPS data of the lithium metal anode (Fig. S11) clearly reveal the dynamic

formation and chemical evolution of the solid electrolyte interphase (SEI) on its surface during cycling. In the open-circuit voltage (OCV) state after cell assembly (Fig. S11(a-d)), an initial SEI has already formed on the lithium anode surface. The C 1s spectrum shows peaks for C-C, C=O, and C-O species originating from the reduction of the DME/DOL solvent. The F 1s spectrum exhibits a pronounced LiF peak (~685 eV) and a -CF_2 peak attributed to the reductive decomposition of the LiTFSI salt (cleavage of -CF_3 groups). The Li 1s spectrum confirms the coexistence of inorganic compounds such as LiF, Li_2CO_3, and Li_2O. The S 2p spectrum already shows signals from sulfur-containing species like SO_3^{2-}/SO_4^{2-}, indicating that sulfur species derived from FeS_2 (possibly via slight dissolution or chemical interaction) have diffused to the anode and been partially oxidized even at OCV.

Upon discharging to 1.0 V (Fig. S11(e-h)), which corresponds to the deep reduction of FeS_2 to Fe and Li_2S, the S 2p spectrum displays intense characteristic doublets for Li_2S and polysulfides (Li_2S_2) in the ~161-163 eV region, along with SO_x peaks at ~168-169 eV. This provides the most direct evidence of polysulfide (LiPS) shuttle effect, the soluble LiPSs generated from FeS_2 reduction migrate to the anode and are reduced to solid Li_2S deposits. Meanwhile, the LiF signals in the F 1s and Li 1s spectra increase significantly, indicating continued decomposition of LiTFSI during discharge, which reinforces the inorganic SEI framework dominated by LiF. The appearance of the C-F peak in the C 1s spectrum further confirms the formation of fluorine-containing organics. These data collectively demonstrate that the discharge process not only intensifies electrolyte decomposition (producing LiF) but also

introduces the critical side-product Li_2S resulting from the shuttle effect.

When charged to 3.0 V (Fig. S11(i-l)), the Li 1s spectrum shows a marked decrease in the intensity of the peak representing Li_2S_2 (~55 eV), indicating that part of the deposited Li_2S_2 is oxidized and migrates back to the cathode. In contrast, the peaks for LiF (~55.8 eV) and Li_2CO_3 (~55.0 eV) remain strong and stable, suggesting that the inorganic SEI components formed from electrolyte decomposition exhibit dynamic stability during cycling, which is crucial for protecting the lithium metal anode.

Fig. S12 presents the XPS data of the FeS_2 cathode, which provides strong support for analyzing the bulk reaction reversibility and interfacial side reactions. At the open-circuit potential (OCV, Fig. S12(a-d)), the S 2p spectrum is dominated by signals from surface oxidation products (sulfate/sulfite species at higher binding energies), while the characteristic peaks of the intrinsic $[S_2]^{2-}$ dimers (~162.5 eV) are obscured. The Fe 2p spectrum shows Fe^{2+} signatures, though the signal may also be influenced by surface oxidation. The presence of C=O, SO_x, and weak LiF peaks confirms the existence of a native surface layer resulting from adsorption and slight oxidation.

Upon discharging to 1.0 V (Fig. S12(e-h)), the intensity of the original FeS_2 (S_2^{2-}) peaks in the S 2p spectrum decreases substantially. Dominant peaks now appear at ~160.5/161.7 eV corresponding to Li_2S and at ~162/163 eV corresponding to polysulfides (Li_2S_x). Simultaneously, the SO_4^{2-} peak at ~168 eV is significantly enhanced. In the Fe 2p spectrum, a characteristic peak of metallic Fe^0 emerges around

~706.5 eV. These changes confirm the reaction mechanism of the Li/FeS_2 battery during discharge: $FeS_2 \rightarrow Li_2S + Fe$. The enhancement of the SO_4^{2-} signal indicates the occurrence of irreversible oxidation of sulfur species by the electrolyte as a side reaction during discharge.

When charged to 3.0 V (Fig. S12(i-l)), the data at this state are key to verifying cathode reversibility and interfacial stability. In the S 2p spectrum, the intensities of the Li_2S and polysulfide peaks are significantly reduced compared to the discharged state, while the characteristic FeS_2 (S_2^{2-}) peaks are notably recovered. In the Fe 2p spectrum, the Fe^0 peak weakens or even disappears, whereas the Fe^{2+} peak (corresponding to FeS_2) strengthens. This directly and strongly proves the reversible reaction: $Li_2S + Fe \rightarrow FeS_2$. The regeneration capability of the FeS_2 host structure is the cornerstone of its intrinsic electrochemical stability. Concurrently, the SO_4^{2-} peak in the S 2p spectrum persists, and the O 1s spectrum shows pronounced peaks for O=C=O (carbonate), -OH, and SO_4^{2-}. This reveals ongoing side reactions at the cathode/electrolyte interface during high-voltage charging, including oxidation of the electrolyte solvent and deep oxidation of active sulfur to form irreversible sulfates. These side products constitute the cathode electrolyte interphase (CEI), which is responsible for irreversible active-material loss and increased impedance.

XPS data confirm two key findings regarding the battery's interfacial evolution. On the lithium anode, the SEI composition dynamically evolves, LiF primarily originates from continuous LiTFSI decomposition, while the appearance and subsequent weakening of Li_2S signals directly prove the shuttle, reduction, and partial

re-oxidation of polysulfides from the FeS_2 cathode. For the FeS_2 cathode, the data conclusively demonstrate the excellent bulk reversibility of the $FeS_2 \leftrightarrow Fe + Li_2S$ conversion reaction. However, persistent sulfate and carbonate signals reveal irreversible interfacial side reactions during high-voltage charging, forming a cathode electrolyte interphase (CEI) that contributes to capacity fade.

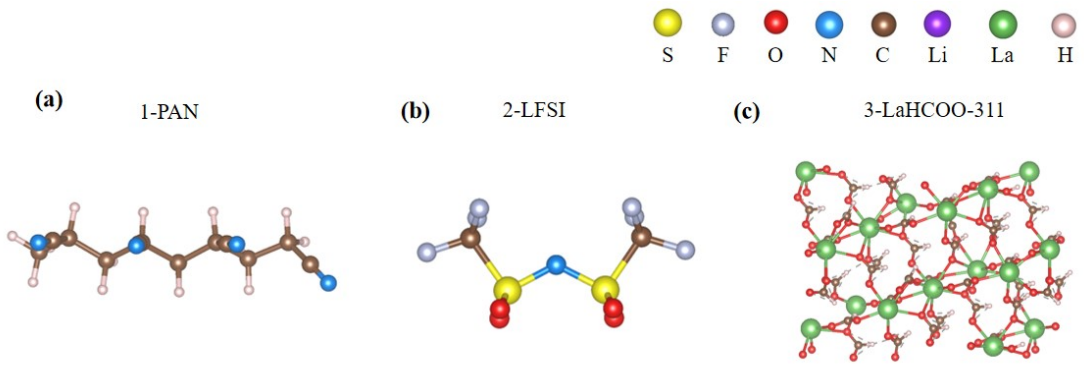

Fig. S13 Structural diagrams of three substances: (a) PAN, (b) LFSI, (c) $LaHCOO^-$

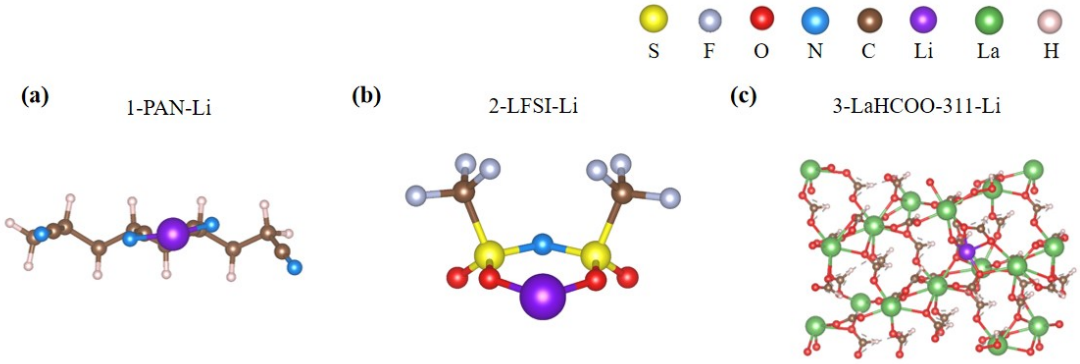

Fig.S14 Structural diagrams of three substances after stable binding with lithium salts:

(a) PAN-Li, (b) LFSI-Li, (c) $LaHCOO_3$-Li

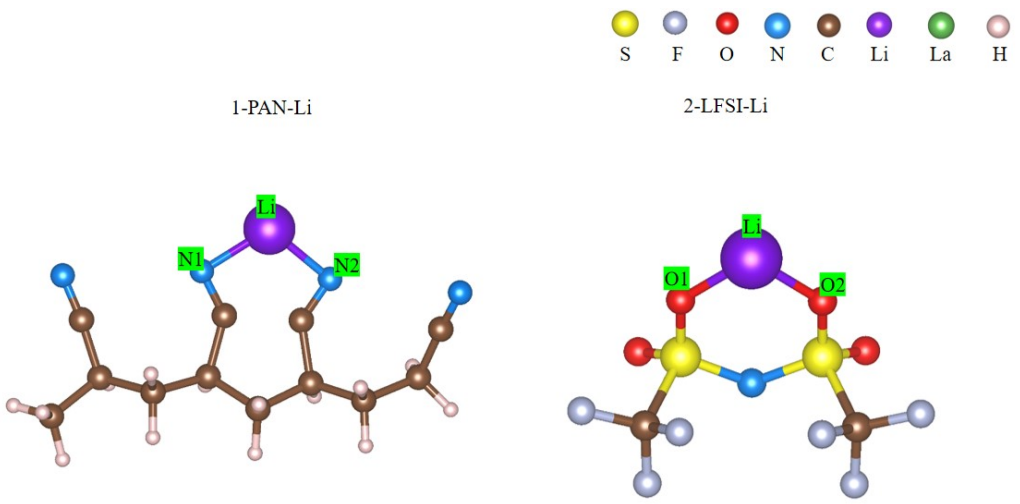

Fig. S15 Structural diagram of PAN interacting stably with lithium salt at nitrogen sites Structural diagram of LFSI interacting with lithium at oxygen sites.

Table S9 Comparison of adsorption Energies for Solid Electrolytes and System Energy Calculations

configuration	Total Energy/eV	Ground state energy/eV	Molecular Energy/eV	Adsorption energy/eV
1-PAN-Li	-192.124	-190.302	-1.986	0.163
2-LFSI-Li	-87.575	-81.406	-1.986	-4.183
3-LaHCOO-311-Li	-891.612	-884.128	-1.986	-5.498

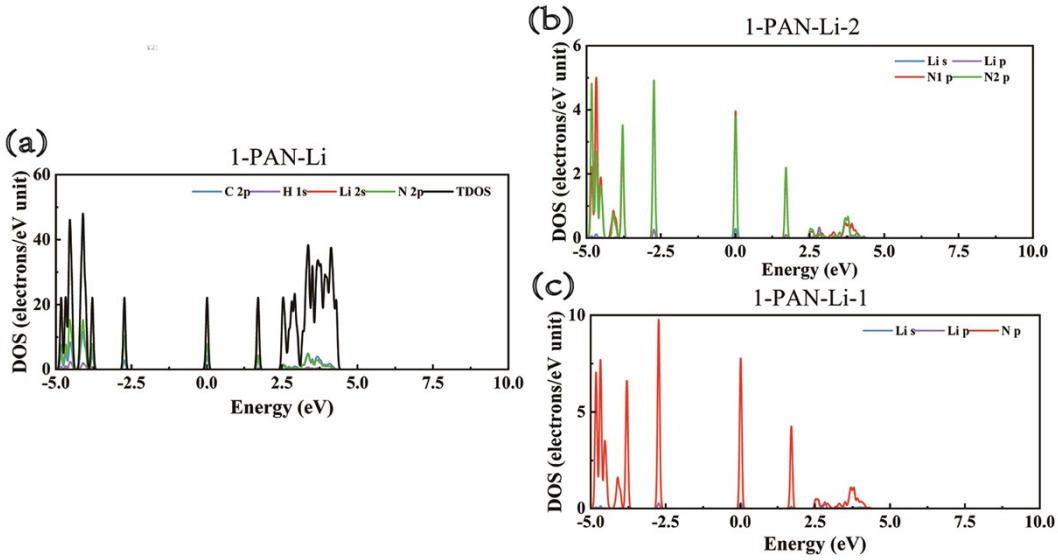

Fig. S16 DOS and PDOS of PAN and Lithium Salts

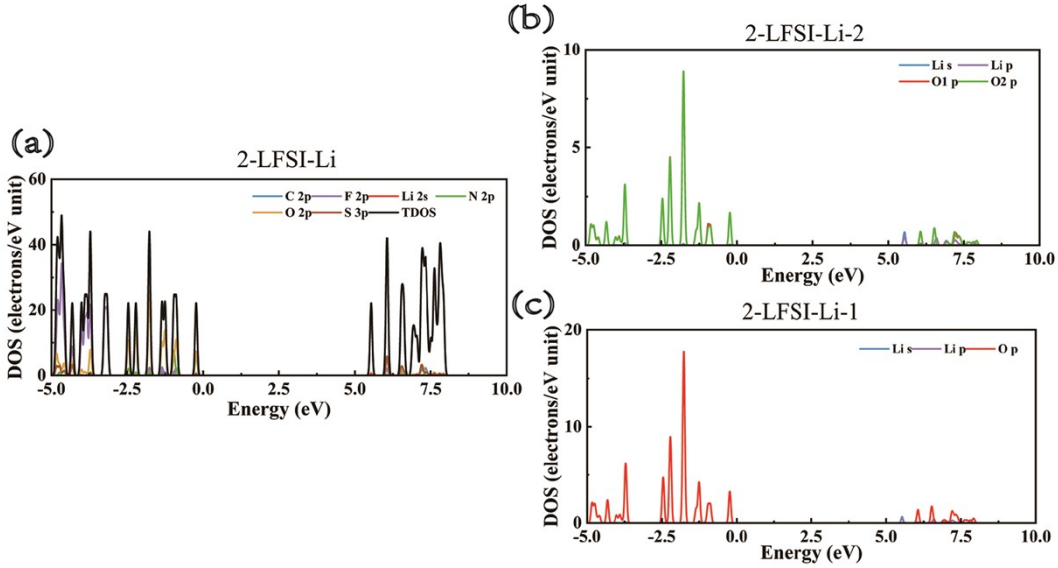

Fig. S17 $LFSI^-$ and Lithium DOS and PDOS

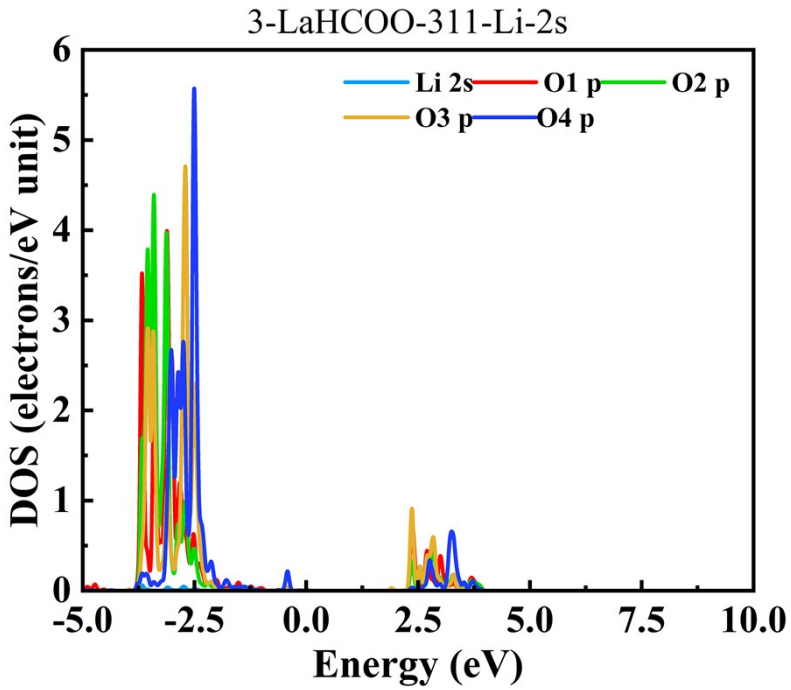

Fig. S18 presents the partial density of states (PDOS) of 3-LaHCOO-311-Li-2s, focusing on the electronic states of Li-2s, and Op (different O orbitals)

The Li-related orbitals (blue) exhibit a pronounced peak below the Fermi level, indicating partial charge transfer of Li^+-consistent with the charge depletion observed in **Fig. S18** and the formation of weak ionic bonds. The O-related orbitals (red) display distinct peaks in the low-energy region (< -2.5 eV), corresponding to the electronic states that arise when O atoms from $TFSI^-$ form O-H covalent bonds with H atoms from the MOF. These bonding states further refine the understanding of the Li^+-MOF and $TFSI^-$-MOF interactions, revealing the equilibrium mechanism in which Li^+ is dissociated but not completely free, while $TFSI^-$ is anchored yet does not hinder ionic conduction.

References:

[1] SAINT, Version 7.60A, Bruker Analytical X-ray Instruments, Inc., Madison, WI, 2008.

[2] Sheldrick, G. M. A Short History of SHELX. Acta Crystallogr. A 2008, 64, 112-122.

[3] Dolomanov, O. V.; Bourhis, L. J.; Gildea, R. J.; Howard, J. A. K.; Puschmann, H. OLEX2: A Complete Structure Solution, Refinement and Analysis Program. J. Appl. Crystallogr. 2009, 42, 339-346.

[4] Spek, A. L. Single-crystal Structure Validation with the Program PLATON. J. Appl. Crystallogr. 2002, 36, 7-13

[5] C. Shen, Y. Liu, Y. Shi, X. Liu, Y. Jiang, S. Huang, J. Zhang, B. Zhao, A multifunctional hydrogel-based triple-network electrolyte for high-performance flexible supercapacitor. J. Colloid Interface Sci. 2024, 653, 85-93

[6] W. Liu, Y. Zhao, C. Yi, W. Hu, J. Xia, Y. Li, High-Performance Aqueous Zinc-Ion Batteries Enabled by Rational Design of MnO_2 Cathode and Electrolyte.J. Liu, Energy Environ. Mater.2024, 7, 12719-12728.

[7] R. Wang, Z. Wu, C. Yu, C. Wei, L. Peng, L. Wang, S. Cheng, J. Xie,Front. Synergistic Effect of Binder and Conductive Additive on the Electrochemical Performance of Silicon-Based Anodes for Lithium-Ion Batteries. Energy Res. 2023, 10, 789-803

[8] G. F. Dewald, Z. Liaqat, M. A. Lange, W. Tremel, W. G. Zeier, Tuning the Ionic and Electronic Conductivity in the Sodium Superionic Conductor Na_3SbS_4 via Lattice Strain and Site Disorder. Angew.Chem., Int. Ed. 2021, 60, 17952-17970

[9] Z. Wu, W. Zhang, Y. Xia, H. Huang, Y. Gan, X. He, X. Xia, J. Zhang, Regulating the solvation structure of electrolyte enables high-voltage and high-performance

Zn-organic batteries. EcoMat 2023, 5, 327-339

[10] P. Lu, Y. Xia, Y. Huang, Z. Li, Y. Wu, X. Wang, G. Sun, S. Shi,Z. Sha, L. Chen, H. Li, F. Wu, Adv. Funct. A Universal Strategy for Constructing Robust Interface Films with Anion–Solvent Coordination for High-Voltage Lithium Metal Batteries. Mater. 2023, 33, 1211-1236

[11] C. Shen, L. Hu, H. Tao, Y. Liu, Q. Li, W. Li, T. Ma, B. Zhao, J. Zhang,Y. Jiang, J. Interfacial engineering of bimetallic sulfides coupled with graphene for enhanced oxygen evolution reaction. Colloid Interface Sci. 2024, 666, 444-454